



Article

Molarity Effects of Fe and NaOH on Synthesis and Characterisation of Magnetite (Fe_3O_4) Nanoparticles for Potential Application in Magnetic Hyperthermia Therapy

Lokesh Srinath Ganapathe, Jamal Kazmi , Mohd Ambri Mohamed , and Dilla Duryha Berhanuddin *

Institut Kejuruteraan Mikro dan Nanoelektronik (IMEN), Universiti Kebangsaan Malaysia (UKM), Bangi 43600, Selangor, Malaysia

* Correspondence: dduryha@ukm.edu.my

Abstract: In this study, the effect of molarity on the structural, magnetic, and heat dissipation properties of magnetite nanoparticles (MNPs) was investigated to optimise the parameters for potential application in magnetic hyperthermia therapy (MHT). MHT works based on the principle of local temperature rise at the tumour site by magnetic iron oxide nanoparticles (MIONPs) with the application of an alternating magnetic field. MHT is a safe method for cancer treatment and has minimal or no side effects. Magnetite (Fe_3O_4) is the best material among MIONPs to be applied in local MHT due to its biocompatibility and high saturation magnetisation value. MNPs were prepared by co-precipitation at varying molarity. Structural characterisation was performed via X-ray powder diffraction (XRD) for crystalline structure analysis and field-emission scanning electron microscopy (FESEM) for morphology and particle size analysis. Measurement of the magnetic properties of the as-synthesised MNPs was carried out using a vibrating sample magnetometer (VSM). Power loss (P) was determined theoretically. The increase in molarity resulted in significant effects on the structural, magnetic, and heat dissipation properties of MNPs. The particle size and saturation magnetisation (M_s) decreased with the gradual addition of base but increased, together with crystallinity, with the gradual addition of iron source. M3 recorded the smallest crystalline size at 3.559 nm. The sample with the highest molarity (M4) displayed the highest heat generation capacity with a p value of up to 0.4056 W/g. High p values at the nano-scale are crucial, especially in local MHT, for effective heat generation, thus proving the importance of molarity as a vital parameter during MNP synthesis.



Citation: Ganapathe, L.S.; Kazmi, J.; Mohamed, M.A.; Berhanuddin, D.D. Molarity Effects of Fe and NaOH on Synthesis and Characterisation of Magnetite (Fe_3O_4) Nanoparticles for Potential Application in Magnetic Hyperthermia Therapy. *Magnetochemistry* **2022**, *8*, 161.

<https://doi.org/10.3390/magnetochemistry8110161>

Academic Editor: Karim Zehani

Received: 20 September 2022

Accepted: 18 November 2022

Published: 21 November 2022

Publisher's Note: MDPI stays neutral with regard to jurisdictional claims in published maps and institutional affiliations.



Copyright: © 2022 by the authors. Licensee MDPI, Basel, Switzerland. This article is an open access article distributed under the terms and conditions of the Creative Commons Attribution (CC BY) license (<https://creativecommons.org/licenses/by/4.0/>).

1. Introduction

Hyperthermia therapy in cancer treatment is well-established and is one of the most promising biological applications of magnetite nanoparticles (MNPs) [1–3]. This treatment induces heat into cancer tissues at a temperature ranging between 41 °C to 46 °C. Hyperthermia treatment will result in a phenomenal effect known as cell apoptosis and necrosis. Cell apoptosis prevents further growth of cancer cells; it does not lead to death of cancer cells but only places them in a stagnant state. Cell apoptosis typically occurs at ~43 °C. Necrosis is the complete annihilation of cancer cells (most or complete death of all cancer cells) and occurs at 45 °C and above [4,5]. In general, cancer cells have a selectively higher sensitivity towards heat and smaller cooling effects than normal cells [6,7]. Hyperthermia therapy is an external approach that produces minimal side effects compared with radiotherapy and chemotherapy [8].

The utilisation of magnetic iron oxide nanoparticles (MIONPs) in the biological field has been a subject of interest in recent years [9–13], including in magnetic hyperthermia therapy (MHT) [14,15]. In MHT, biocompatible MIONPs are introduced at the tumour site by magnetic targeting, followed by heat generation by exposure to alternating magnetic field [1,8,16–20]. MHT governs the conversion principle of electromagnetic energy into

heat energy to stimulate a local temperature rise [14,21]. This technology has managed to increase the effectiveness of the treatment and has a reduced collateral damage on the surrounding healthy tissues [22].

The selection of the correct and suitable MIONPs for local MHT is a crucial step to ensure their effectiveness in the biological field. Materials with high magnetic properties, such as Co and Ni, are toxic and are unsuitable for medical application. Magnetite nanoparticles (MNP) are a safe and promising candidate in MHT application due to its biocompatibility, excellent magnetic property and stable magnetic response compared with the other types of MIONPs [23–27]. Additionally, MNPs possess superparamagnetism, which means that particles lose their magnetisation without magnetic field application, thereby reducing the risk of particle aggregation [28]. Several studies have reported on the magnetic properties and structure of MNPs doped with tin and magnesium. Doped MNPs can be experimented in targeted drug delivery and magnetic resonance imaging contrast agents due to their ultrafine crystalline size, low coercivity, and high saturation magnetisation [29]. However, these materials are yet to be tested for in vivo applications, especially in MHT.

A number of approaches can be used to obtain MHT-applicable MNPs by altering their synthesis parameters. For example, the heat and pressure parameters of hydrothermal method are tailored to obtain MHT-applicable MNPs [30]. Thermal decomposition has very good control over nanoparticle shapes and leads to a very narrow size distribution of nanoparticles to obtain the desired shape anisotropy, such as nanocubes and nanorods. The shape design of MNPs is a major aspect in synthesis of various nanostructures with unique biocompatibility and magnetic properties [31]. Co-precipitation is the most commonly used method in the synthesis of MNPs because of its affordability and simplicity; in this method, two separate iron sources are mixed simultaneously in the presence of a base [32,33]. Nevertheless, the molarity of iron source and base influences the structural and magnetic properties of MNPs, significantly affecting the heat dissipation of MNPs in MHT. An appropriate amount (molarity) of iron source and base should be identified to yield MNPs with high heat generation capability for MHT.

In this study, MNPs were prepared by co-precipitation, where the molarity of iron salts and base was varied to determine the effect on the structural, magnetic and heat generation properties for potential application in local MHT. With the variations in molarity, high power loss (P) values should be generated for excellent MHT. Results show that synthesis of MNPs with the right molarity values for iron salts and base is important in the high-power loss (P) by using a theoretical determination (as further discussed in the sections below) through a vibrating sample magnetometer (VSM) for effective heat generation in MHT.

2. Methodology

MNPs were synthesised through co-precipitation of Fe^{2+} and Fe^{3+} at a molar ratio of 2:1. Sodium hydroxide (NaOH) was used as the base. The iron source was first prepared by dissolving 1.28 M $\text{FeCl}_3 \cdot 6\text{H}_2\text{O}$ and 0.64 M $\text{FeCl}_2 \cdot 4\text{H}_2\text{O}$ into 0.4 M hydrochloric acid (HCl), which was then diluted to 25 mL with deionised water. HCl was added to neutralise the anionic charges. The base solution was prepared by dissolving 1.5 M NaOH into 250 mL of deionised water under vigorous magnetic stirring and nitrogen gas (N_2) atmosphere protection in a reaction vessel. This step was done to create a non-oxidising atmosphere to avoid the oxidation of the iron source. The prepared iron source was added dropwise into the reaction vessel containing the base solution. The mixture was labelled as M1. The entire reaction occurred under an N_2 atmosphere, with a stirring rate of 1500 rpm and reaction temperatures of 25 °C for 30 min. At the end of the reaction, the observed black precipitates were collected and centrifuged at 4000 rpm for 15 min. The black precipitates were collected and washed with ethanol and deionised water several times. The precipitates were then dried in an oven at 70 °C overnight. The dried black granules were finely ground into powdered form. The flow chart of the entire experiment is illustrated in Figure 1.

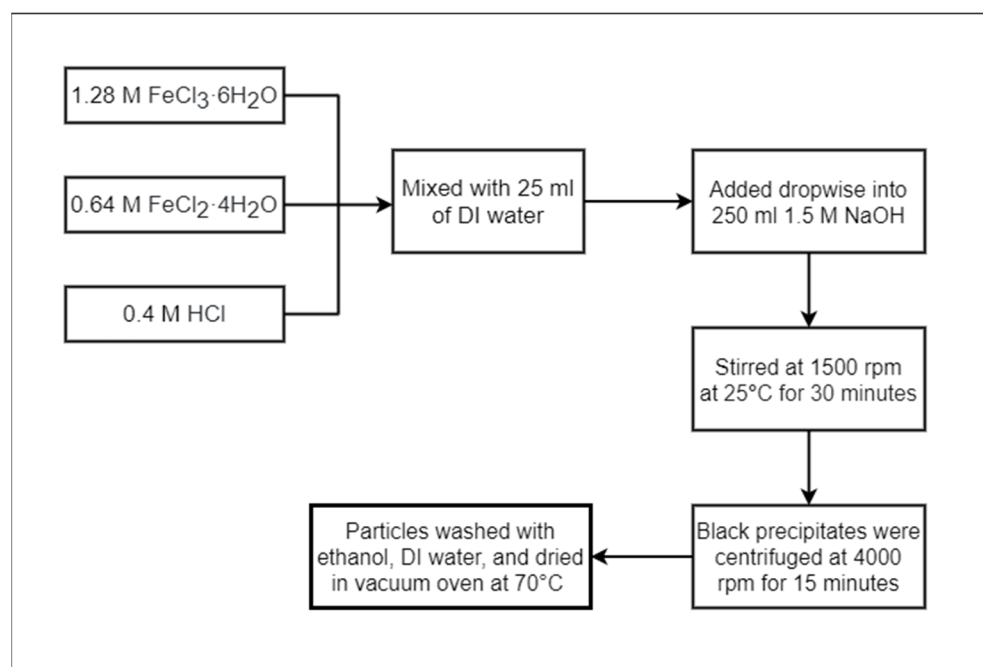


Figure 1. Flowchart of the synthesis of core magnetite nanoparticles.

The entire process was repeated by varying (increasing) the molarities (M2, M3, and M4) of the iron sources ($\text{FeCl}_3 \cdot 6\text{H}_2\text{O}$ and $\text{FeCl}_2 \cdot 4\text{H}_2\text{O}$) and the base (NaOH). The detailed molarity values are shown in Table 1a.

Table 1. (a) Molarity values of $\text{FeCl}_3 \cdot 6\text{H}_2\text{O}$, $\text{FeCl}_2 \cdot 4\text{H}_2\text{O}$, and NaOH for samples M1 to M4. (b) Molarity values of $\text{FeCl}_3 \cdot 6\text{H}_2\text{O}$, $\text{FeCl}_2 \cdot 4\text{H}_2\text{O}$, and NaOH for samples C1 to C4.

Samples	Iron Source		Base
	$\text{FeCl}_3 \cdot 6\text{H}_2\text{O}$	$\text{FeCl}_2 \cdot 4\text{H}_2\text{O}$	
M1	1.28	0.64	1.5
M2	1.75	0.875	2.0
M3	2.00	1.00	2.5
M4	2.56	1.28	3.0

Samples	Iron Source		Base
	$\text{FeCl}_3 \cdot 6\text{H}_2\text{O}$	$\text{FeCl}_2 \cdot 4\text{H}_2\text{O}$	
C1	1.75	0.875	1.5
C2	2.00	1.00	1.5
C3	2.56	1.28	1.5
C4	3.2	1.6	1.5

The second batch of samples was prepared, where only the iron sources ($\text{FeCl}_3 \cdot 6\text{H}_2\text{O}$ and $\text{FeCl}_2 \cdot 4\text{H}_2\text{O}$) were varied while the base (NaOH) was kept constant. This batch of samples was used to analyse whether iron source alone will affect the structural and magnetic properties of MNPs and consequently influence the heat generation capacity, which is crucial in MHT application. The step is important to determine the appropriate molarity for producing potential MNPs for MHT application. The solution mixtures were labelled as C1, C2, C3, and C4, and their molarity details are shown in Table 1b.

X-ray powder diffraction (XRD) characterisation was carried out using a Bruker D8 Advance X-ray Diffractometer (XRD) with a 2θ angle of 10° – 80° and Cu-K α radiation

($\lambda = 1.5406 \text{ \AA}$) to identify the structure and phase of the synthesised MNPs. Field-emission scanning electron microscopy (FESEM) analysis was conducted on Zeiss-MERLIN FESEM to investigate the morphology and topology of the synthesised MNPs. The magnetic properties of the synthesised MNPs were analysed using a Lakeshore 7404 vibrating sample magnetometer (VSM) at room temperature under an applied magnetic field (H) up to 14 kOe with a frequency (f) of 80 Hz. The H was applied horizontally to the sample (in-plane method).

Magnetic hysteresis loss (power loss of MNPs) was calculated via a theoretical approach using the $M-H$ curve obtained from VSM. The amount of heat generated by the synthesised MNPs can be calculated using the following equation [20].

$$P(\text{W/g}) = [f \oint H dB] \times 10^{-7}, \quad (1)$$

where f is the frequency, H is the applied magnetic field, and B is the magnetisation of MNPs in H . The area of the hysteresis loop in H is expressed as $\oint H dB$. Therefore, in our calculations, the f value is 80 Hz, and the expression $\oint H dB$ is replaced for the area of the hysteresis loop calculated under 14 kOe by using VSM.

3. Results and Discussion

The colour of the obtained samples prepared by co-precipitation was black (Figure 2). This finding proved that the obtained samples were magnetite (Fe_3O_4) and not maghemite ($\gamma\text{-Fe}_2\text{O}_3$), which has a brown appearance. Furthermore, the identifying colour of magnetite (Fe_3O_4) is black [25]. The colour of the obtained samples could be used for physical determination of the synthesised samples. Akhirudin et al. reported that black precipitates (magnetite) were oxidised, which resulted in a colour change from black to brown, indicating the formation of $\gamma\text{-Fe}_2\text{O}_3$ (maghemite) saturated suspension [34].

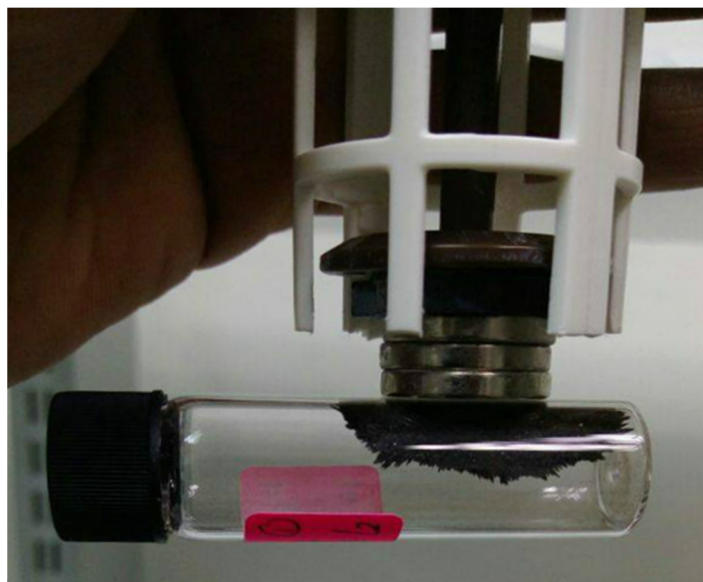


Figure 2. Response of synthesised MNPs under external magnetic field.

The synthesised MNPs possess magnetite characteristics (Figure 2), where the black-coloured sample powder in the sample bottle became attracted upon contact with an external magnetic field. This finding proved the ferromagnetism characteristics of the synthesised black-coloured powder [25,35].

The yield significantly increased by up to 3.5 times by increasing the molarity from M1 to M4 and by 1.8 times from C1 to C4. Hence, the base (NaOH) is a major contributing factor towards the higher yield of MNPs.

Figure 3 shows the XRD patterns of the synthesised MNPs at increasing molarities for M1 to M4 and C1 to C4, respectively. The main relative intensities and position of all diffraction peaks at 30.10° , 35.43° , 42.99° , 53.66° , 57.29° , 62.67° , 67.62° , and 75.80° (2θ degree) with the planes of (220), (311), (400), (422), (511), (440), (531), and (622), respectively, are in agreement with the standard pattern for JCPDS Card No. (19-0629) indexed magnetite (Fe_3O_4) phase with an inverse spinel structure [36–40]. In the (311) plane, the synthesised MNPs illustrate very broad peaks that indicate low crystallinity. This finding is in contrast to bigger and well-crystallised samples that exhibit narrower peaks with higher intensity. The XRD peaks are usually not well-developed compared with the bulk samples due to the ultra-fine size of MNPs. As shown in Figure 3a, the crystallinity of MNP does increase as the molarity of the reactant increases until M3. In M4, the crystalline peak formed starts to deteriorate and too many particles are formed [25,28]. These excess particles distort the angle formation of the crystalline structure [41,42]. The crystallite size continuously grows in C1 to C4 (Figure 3b). These findings suggested that base, in this case, NaOH, is an important factor in the crystalline growth formation of MNPs.

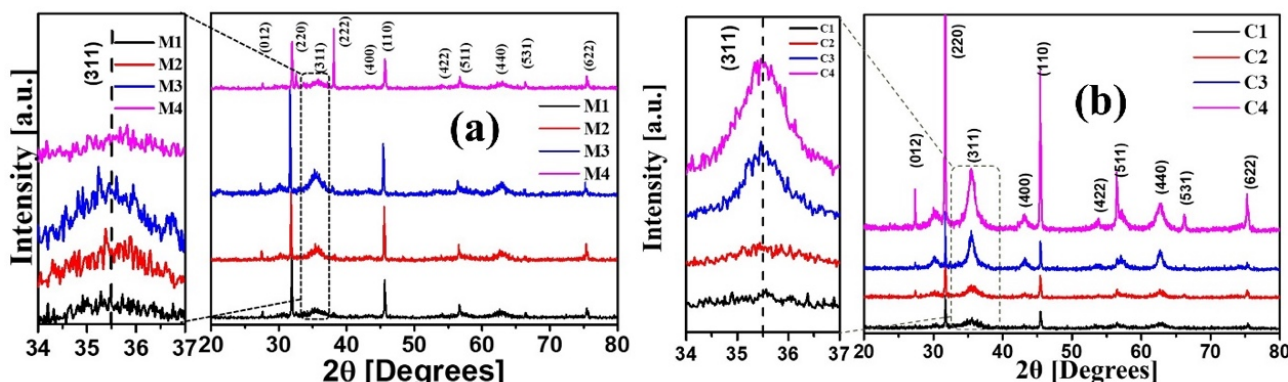


Figure 3. XRD pattern of MNPs synthesised at increasing molarities; (a) from M1 to M4 and (b) from C1 to C4.

The crystalline sizes of the synthesised MNPs were determined from the full-width half-maximum (FWHM) for the main diffracted peak at (311) based on the Debye–Scherer's equation [43–45].

$$\text{FWHM} (2\theta) = \frac{K\lambda}{L \cos\theta} \quad (2)$$

where K is the Scherer's constant (shape factor) ($K = 0.89$), λ is the wavelength ($\lambda = 1.5406 \text{ \AA}$), L is the crystallite size (in nanometres), and θ is the Bragg's angle (in radians). Table 2a,b show the Bragg's angle, FWHM, and crystallite size values for both sets of samples.

The FWHM values for both sets of samples were generated via Origin 2019b (9.65) software. These results showed that the obtained MNPs are all in the nano-scale, with M3 recording the smallest value of 3.559 nm.

Figures 4 and 5 show the FESEM images of MNPs synthesised at increasing molarities. In general, aggregates, rather than single-core MNPs, were formed due to agglomeration, which will be discussed later in this section. In Figure 4, the aggregate morphology of the MNPs becomes distorted with increasing molarities of the iron sources and base. Cubical MNPs were observed in M2, M3, and M4, which lose their cubical shape as the molarities of the iron sources and base increase. In Figure 5, the very same scenario was observed. The aggregate morphology of the MNPs becomes distorted with increasing molarities of the iron sources while keeping the base constant. C1 also possesses a cubical shape. Hence, the molarity of the iron sources and base plays an important role in maintaining the aggregate morphology of the MNPs.

Table 2. (a) Brag's angles, FWHM and crystallite sizes for samples M1 to M4. (b) Bragg's angles, FWHM, and crystallite sizes for samples C1 to C4.

(a)					
Samples	2θ (°)	θ (Rad)	FWHM	Crystallite Size (nm)	$(h k l)$
M1	35.56	0.3103	1.974	3.832	(3 1 1)
M2	35.52	0.3099	1.674	4.520	(3 1 1)
M3	35.45	0.3094	2.103	3.599	(3 1 1)
M4	35.69	0.3115	1.042	7.260	(3 1 1)

(b)					
Samples	2θ (°)	θ (Rad)	FWHM	Crystallite Size (nm)	$(h k l)$
C1	35.48	0.3096	1.859	4.070	(3 1 1)
C2	35.63	0.3109	1.604	4.716	(3 1 1)
C3	35.51	0.3099	0.9694	7.805	(3 1 1)
C4	35.52	0.3100	1.282	5.902	(3 1 1)

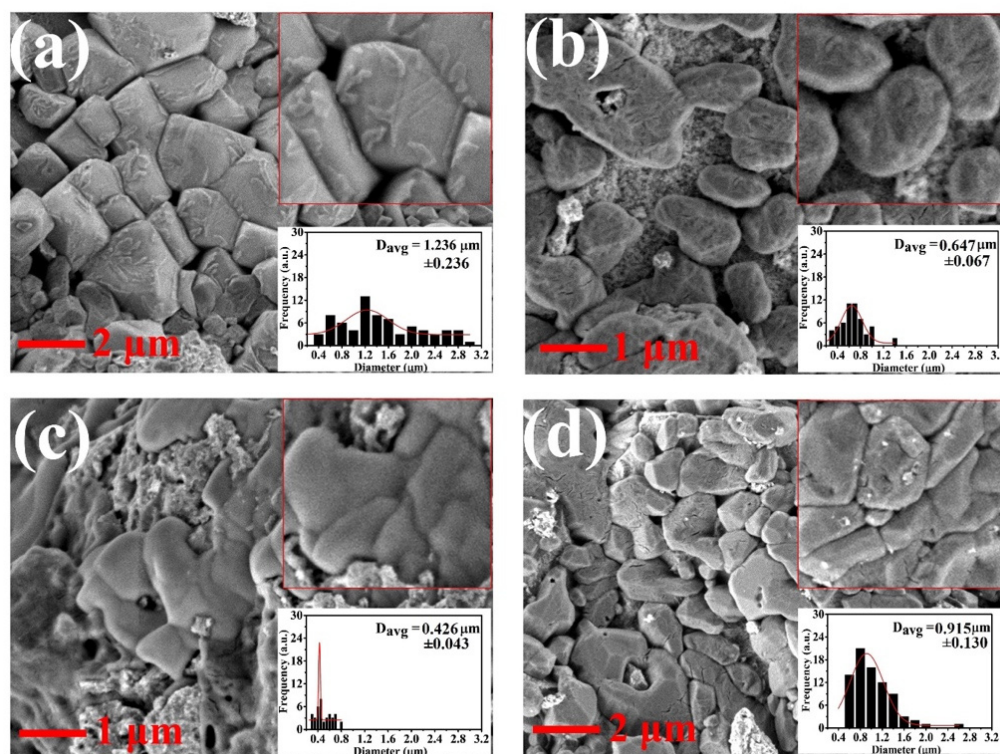


Figure 4. FESEM images of MNPs synthesised at increasing molarities: [(a) M1; (b) M2; (c) M3; and (d) M4].

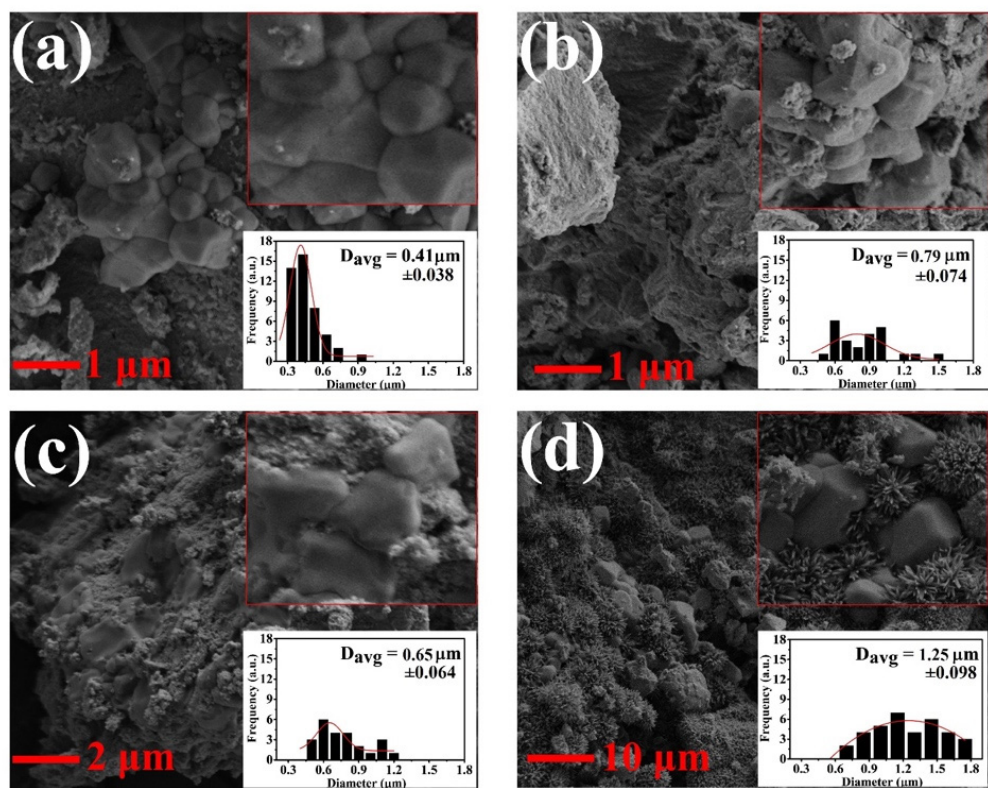


Figure 5. FESEM images of MNPs synthesised at increasing molarities: [(a): C1; (b): C2; (c): C3; and (d): C4].

In terms of aggregate size of MNPs, the average diameter of MNPs was calculated by ImageJ software Version 1.53t. The error of margins was calculated in MS Excel 2019 by using the following equation [46–48].

$$\text{Margin of error} = \text{Confident.T}(\alpha, \text{SD}, N) \quad (3)$$

where α is the confident percentage (set to be 95% or 0.05) and N is the number of values. The average diameters of MNPs for M1 to M4 are 1.236, 0.657, 0.426, and 0.915 μm , respectively. In general, the aggregate size decreases with a gradual increase in molarity. Similarly, Guo et al. [49] reported that the particle size reduces as the molarity of the base NaOH increases.

In Figure 5, the average diameters of MNPs from C1 to C4 are 0.41, 0.79, 0.65, and 1.25 μm . In this case, the aggregate size of MNPs generally increases. With increasing molarities of both iron sources, more materials are available for the growth phase, leading to the synthesis of aggregates with larger diameters [39]. This trend is congruent with the findings of Schwaminger et al. [50–52].

For M1 to M4, MNPs are mostly uniformly distributed (Figure 4). More intense agglomeration of MNPs occurred in C1–C4 (Figure 5). This finding could be due to the magnetic interaction, usually of a dipole nature between the nanoparticles [20]. In particular, MIONPs are very prone to agglomeration in the absence of a capping agent. In the present experiment, such an agent was not applied, so the efficacy level of bare MNPs can be determined. The aggregate size of the synthesised MNPs is larger than those in other reported works. The use of co-precipitation for synthesis has poor control over particle distribution and is susceptible to agglomeration [53–56]. Felisa et al. and Zohreh et al. utilised hydrothermal and thermal decomposition, respectively, which have good control over the size of the synthesised particles [57,58]. However, these approaches are often expensive and time-consuming. The ferromagnetism property from our technique is

discussed later in this paper, which proves that the particles definitely exhibit nanoparticle behaviour.

In conclusion, the molarity of iron sources ($\text{FeCl}_3 \cdot 6\text{H}_2\text{O}$ and $\text{FeCl}_2 \cdot 4\text{H}_2\text{O}$) and base (NaOH) plays a crucial role in the aggregate size of MNPs. The aggregate size of MNPs is reduced with increasing molarity of the base (NaOH) but increased with increasing molarity of the iron sources ($\text{FeCl}_3 \cdot 6\text{H}_2\text{O}$ and $\text{FeCl}_2 \cdot 4\text{H}_2\text{O}$). The uniformly distributed MNPs make them desirable in the biomedical field, especially in MHT applications [59].

The magnetic properties of the synthesised MNPs are illustrated in Figure 6a,b and Table 3a,b. Figure 6a and Table 3a present MNPs from M1 to M4, whereas Figure 6b and Table 3b present MNPs from C1 to C4. According to Figure 6a,b, all samples display ferromagnetic properties. In both cases, the M_s values of all samples are lower than that of the bulk magnetite (92 emu/g). This finding could be due to the disordered magnetic spins on the surface of MNPs, which are caused by incomplete coordination number [20,38,60]. It could also be due to the breakdown of exchange bonds at a massive scale for surface atoms [39]. Additionally, the aggregation of multiple crystallites forms large magnetic core of MNPs that may have cation vacancies (formed during synthesis), thereby reducing the M_s ; by contrast, smaller MNPs constitute mainly from individual crystals, where the amount of cation vacancies is reduced, leading to higher M_s values [36].

Table 3. (a) Magnetic properties and power losses of samples (M1–M4). (b). Magnetic properties and power losses of samples (C1–C4).

Samples	(a)			
	Saturation Magnetisation, M_s (emu/g)	Coercivity, H_c (Oe)	Retentivity, M_r (emu/g)	Power Loss, P (W/g)
M1	37.090	33.933	1.2623	0.1239
M2	41.095	33.313	1.2383	0.173
M3	34.318	32.532	1.1104	0.1169
M4	25.804	30.841	0.94617	0.4056

Samples	(b)			
	Saturation Magnetisation, M_s (emu/g)	Coercivity, H_c (Oe)	Retentivity, M_r (emu/g)	Power Loss, P (W/g)
C1	22.977	39.165	0.49263	0.0946
C2	25.705	37.044	0.84604	0.15222
C3	31.411	41.741	2.1619	0.0703
C4	40.531	33.286	1.9561	0.1645

For samples M1 to M4, the M_s values decrease with a gradual increase in molarity because of the thickening of the magnetically dead layer (non-magnetic interfaces) in alkaline media (in this case NaOH) [38,39]. Based on Table 3a, the M_s values increase from M1 to M2 and then start to decrease from M3 to M4. These trends show that M2 ($\text{NaOH} = 2.0\text{ M}$) is the M_s limit; starting from M3 onwards, the production of the non-magnetic interface begins. This explains why the M_s value of M2 is greater than that of M1.

Another main relationship that could be observed is that M_s values decease with decreasing particle size because of the modified cationic distribution and disordered surface. The disordered or canted spins on the surface of MNPs prevent the alignment of the core spins along with the field direction, producing low M_s values for small-sized MNPs [61].

In both situations, the decrease in the particle size increases the surface-to-volume ratio that triggers the production of non-magnetic interfaces. The total magnetisation of MNPs reduces the particle size because of the increase in magnetic integral that finally leads to superparamagnetism. At this state, each particle behaves like a big spin with quelled exchange interaction between particles [38]. These reasons mainly explain the reduction in magnetic moment resulting in low M_s values.

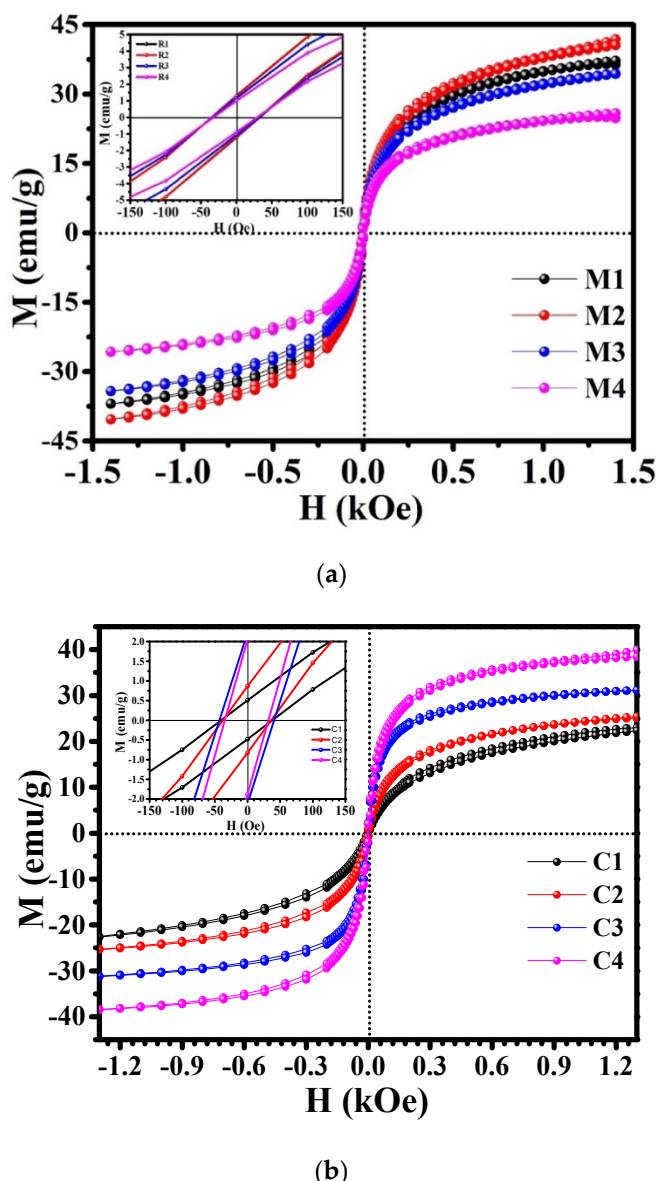


Figure 6. (a) $M-H$ curve of samples M1 to M4. (b) $M-H$ curve of samples C1 to C4.

For samples C1 to C4, the M_s values increase with a gradual increase in the iron source. This finding proves that iron source increases the magnetic property of MNPs. C3 has the highest H_c value of 41.741 Oe and has the biggest crystalline size of 7.805 nm among all the samples.

In both scenarios, the average particle sizes are in the nanometer range, resulting in low H_c values. However, average magnetisation clearly shows magnetic saturation and clear hysteresis, which is a clear sign of ferromagnetism. Among the magnetic properties, the three magnetic properties that play a crucial role in MHT are magnetic anisotropy, M_s value, and superparamagnetism. Magnetic anisotropy deals with the amount of magnetic energy required to rotate dipoles varies depending on the direction. MNPs with high anisotropy should be utilised in MHT. The magnetic anisotropy of the sample can be evaluated by singular point detection (SPD), thermomagnetic measurement systems, and torque magnetometers, which are out of our research scope [56].

Superparamagnetism is also another magnetic property that plays a crucial role in MHT application. Nevertheless, in our case, we successfully managed to synthesise MNPs that are applicable to MHT, even though they were in the ferromagnetic regime, similar to the study of Iacovita et al. [36]. A high M_s value also contributes to efficient MHT

application. However, the obtained M_s values seem to not have any correlation with the obtained p values, which is congruent with the findings of Goya et al. [62].

The shape and size of the hysteresis loop is significant. The area within a hysteresis loop is the magnetic energy loss. This energy loss is expounded as heat energy that is contained within a magnetic sample (in this case, MNPs) and is competent in generating heat (rising the temperature) [38]. The enhanced power loss (P) values in the ferromagnetic regime are ascribed to the synergistic contribution from the susceptibility and hysteresis loss [63]. This concept is of utmost importance for application in the biomedical field, especially in MHT.

Figure 6a,b show the magnetisation curves of the synthesised MNPs at room temperature within an H value of ± 14 kOe as the applied magnetic field. The values of the power losses (P) were calculated according to Equation (1), where f is 80 Hz, and H is 14 kOe were tabulated in Table 3a,b. Based on Equation (1), f is directly proportional to P . Hence, the f value does have a significant impact on P , as proven by Nguyen and Kim [64]. In general, the obtained p values are low as compared to p values obtained by other studies [20,57,58], where the applied f ranges from 100 to 300 kHz. This finding is mainly due to a low-frequency value (80 Hz) applied during the VSM measurement that could not be varied and fixed.

Tong et al. used a frequency value of 325 kHz to obtain P at 1026 W/g [63]. Similarly, if f value of 300 kHz was utilised on sample M4 and by applying it to Equation (1), the obtained p value is 1521 W/g, which is nearly 1.5 times higher at the reduced frequency of 25 kHz. This calculation has proved that the obtained MNPs would definitely be able to deliver such p value at the kHz range. In another similar work, Cervadoro et al. used a frequency range in between 0.2 and 30 MHz [65]. The safe in vivo (application within the human body) range of the used frequencies values for MHT application ranges typically between 100 kHz to 300 kHz [16,53,66].

The synthesised MNPs M1 to M4 possess higher p value than C1 to C4. This could be due to the increment in base molarity (NaOH), which proves to be a great contributing factor towards the generation of heat in MNPs. M4 possesses the highest p value at 0.4056 W/g, making M4 the best candidate among all the other seven samples for the application in local MHT.

4. Conclusions

The structural, magnetic, and heat generation (power loss) properties of as-synthesised MNPs were successfully investigated for potential application in local MHT. As the molarities of the reaction are increased for the first set of experiments, the crystallinity limit of MNPs seems to increase until M3 only. In the second set of an experiment, the crystallinity of the synthesised MNPs continuously increases from C1 to C4. The particle size of MNPs reduces with the increasing base while increases together with the iron source. More uniformly distributed MNPs are formed as well with an increasing base. The M_s values of the synthesised MNPs decrease with increment in base, whereas they increase with increasing iron source. In terms of heat generation (power loss), the MNPs synthesised in the first set of the experiment (M1–M4) have higher p values than the samples synthesised in the second set of the experiment (C1–C4). Among all of the eight synthesised samples, M4 possesses the best heat generation capacity with a p value of 0.4056 (W/g).

In conclusion, the molarity of the iron source and the base does affect the crystallinity, morphology, particle size, M_s , and p values of MNPs, which are essential parameters in biomedical applications, especially for local MHT. The selected potential candidate for application in local MHT is M4 due to its uniformly distributed particles and high p value. Based on the obtained p values in Table 3a,b, higher p values are generated with higher molarities of both iron and base. Therefore, future researchers should apply higher amounts of iron source (C4) and high amount of base (M4) to synthesise MNPs that generate high p values. MNPs with large p values have to be synthesised to ensure better heat dissipation for local MHT.

Author Contributions: Conceptualization: M.A.M. and D.D.B.; Methodology: L.S.G.; Formal analysis and investigation: L.S.G., J.K. and D.D.B.; Writing—original draft preparation: L.S.G.; Writing—review and editing: M.A.M. and D.D.B.; Funding acquisition: D.D.B.; Resources: M.A.M. and D.D.B.; Supervision: M.A.M. and D.D.B. All authors have read and agreed to the published version of the manuscript.

Funding: This work is funded by Universiti Kebangsaan Malaysia under research grant DIP-2019-072.

Institutional Review Board Statement: Not applicable.

Informed Consent Statement: Not applicable.

Data Availability Statement: Not applicable.

Conflicts of Interest: The authors declare that they have no known competing financial interests or personal relationships that could have appeared to influence the work reported in this paper.

References

1. Häring, M.; Schiller, J.; Mayr, J.; Grijalvo, S.; Eritja, R.; Díaz, D. Magnetic Gel Composites for Hyperthermia Cancer Therapy. *Gels* **2015**, *1*, 135–161. [CrossRef] [PubMed]
2. Giustini, A.J.; Petryk, A.A.; Cassim, S.M.; Tate, J.A.; Baker, I.; Hoopes, P.J. Magnetic Nanoparticle Hyperthermia in Cancer Treatment. *Nano LIFE* **2010**, *1*, 17–32. [CrossRef] [PubMed]
3. Moradiya, M.A.; Ladani, A.; Ladani, J.; Raiyani, C.; Markna, J.H. New Way to Treat Cancer: Magnetic Nanoparticle based Hyperthermia. *J. Chem. Sci. Eng. JCSE* **2019**, *2*, 58–60.
4. Azcona, P.; Zysler, R.; Lassalle, V. Simple and novel strategies to achieve shape and size control of magnetite nanoparticles intended for biomedical applications. *Colloids Surf. A Physicochem. Eng. Asp.* **2016**, *504*, 320–330. [CrossRef]
5. Daoush, W.M. Co-Precipitation and Magnetic Properties of Magnetite Nanoparticles for Potential Biomedical Applications. *J. Nanomed. Res.* **2017**, *5*, 00118. [CrossRef]
6. Bonvin, D.; Alexander, D.T.L.; Millán, A.; Piñol, R.; Sanz, B.; Goya, G.F.; Martínez, A.; Bastiaansen, J.A.M.; Stuber, M.; Schenk, K.J.; et al. Tuning properties of iron oxide nanoparticles in aqueous synthesis without ligands to improve MRI relaxivity and SAR. *Nanomaterials* **2017**, *7*, 225. [CrossRef]
7. Macías-Martínez, B.I.; Cortés-Hernández, D.A.; Zugasti-Cruz, A.; Cruz-Ortíz, B.R.; Múzquiz-Ramos, E.M. Heating ability and hemolysis test of magnetite nanoparticles obtained by a simple co-precipitation method. *J. Appl. Res. Technol.* **2016**, *14*, 239–244. [CrossRef]
8. Kobayashi, T. Cancer hyperthermia using magnetic nanoparticles. *Biotechnol. J.* **2011**, *6*, 1342–1347. [CrossRef]
9. Estelrich, J.; Escribano, E.; Queralt, J.; Busquets, M.A. Iron oxide nanoparticles for magnetically-guided and magnetically-responsive drug delivery. *Int. J. Mol. Sci.* **2015**, *16*, 8070–8101. [CrossRef]
10. Estelrich, J.; Antònia Busquets, M. Iron oxide nanoparticles in photothermal therapy. *Molecules* **2018**, *23*, 1567. [CrossRef]
11. Lagrow, A.P.; Besenhard, M.O.; Hodzic, A.; Sergides, A.; Bogart, L.K.; Gavrilidis, A.; Thanh, N.T.K. Unravelling the growth mechanism of the co-precipitation of iron oxide nanoparticles with the aid of synchrotron X-ray diffraction in solution. *Nanoscale* **2019**, *11*, 6620–6628. [CrossRef] [PubMed]
12. Liu, L.; Pu, X.; Yin, G.; Chen, X.; Yin, J.; Wu, Y. Biomimetic mineralization of magnetic iron oxide nanoparticles mediated by bi-functional copolyptides. *Molecules* **2019**, *24*, 1401. [CrossRef] [PubMed]
13. Karim, S.S.A.; Dee, C.F.; Majlis, B.Y.; Mohamed, M.A. Recent progress on fabrication of zinc oxide nanorod-based field effect transistor biosensors. *Sains Malays.* **2019**, *48*, 1301–1310. [CrossRef]
14. Piñeiro, Y.; Vargas, Z.; Rivas, J.; López-Quintela, M.A. Iron Oxide Based Nanoparticles for Magnetic Hyperthermia Strategies in Biological Applications. *Eur. J. Inorg. Chem.* **2015**, *2015*, 4495–4509. [CrossRef]
15. Surowiec, Z.; Miaskowski, A.; Budzyński, M. Investigation of magnetite Fe_3O_4 nanoparticles for magnetic hyperthermia. *Nukleonika* **2017**, *62*, 183–186. [CrossRef]
16. Cassim, S.M.; Giustini, A.J.; Baker, I.; Hoopes, P.J. Development of novel magnetic nanoparticles for hyperthermia cancer therapy. *Energy-Based Treat. Tissue Assess. VI* **2011**, *7901*, 365–374. [CrossRef]
17. Das, R.; Alonso, J.; Nemati Porshokouh, Z.; Kalappattil, V.; Torres, D.; Phan, M.H.; Garaio, E.; García, J.Á.; Sanchez Llamazares, J.L.; Srikanth, H. Tunable High Aspect Ratio Iron Oxide Nanorods for Enhanced Hyperthermia. *J. Phys. Chem. C* **2016**, *120*, 10086–10093. [CrossRef]
18. Engelmann, U.; Buhl, E.M.; Baumann, M.; Schmitz-Rode, T.; Slabu, I. Agglomeration of magnetic nanoparticles and its effects on magnetic hyperthermia. *Curr. Dir. Biomed. Eng.* **2017**, *3*, 457–460. [CrossRef]
19. Kafrouni, L.; Savadogo, O. Recent progress on magnetic nanoparticles for magnetic hyperthermia. *Prog. Biomater.* **2016**, *5*, 147–160. [CrossRef]
20. Li, Z.; Kawashita, M.; Araki, N.; Mitsumori, M.; Hiraoka, M.; Doi, M. Magnetite nanoparticles with high heating efficiencies for application in the hyperthermia of cancer. *Mater. Sci. Eng. C* **2010**, *30*, 990–996. [CrossRef]

21. Soleymani, M.; Khalighfard, S.; Khodayari, S.; Khodayari, H.; Kalhori, M.R.; Hadjighassem, M.R.; Shaterabadi, Z.; Alizadeh, A.M. Effects of multiple injections on the efficacy and cytotoxicity of folate-targeted magnetite nanoparticles as theranostic agents for MRI detection and magnetic hyperthermia therapy of tumor cells. *Sci. Rep.* **2020**, *10*, 1695. [[CrossRef](#)] [[PubMed](#)]
22. do Carmo Paresque, M.C.; de Oliveira, E.M.; Nogueira, D.A.; de Castro, J.A.; de Campos, M.F. Magnetite nanoparticles study applied to magnetic hyperthermia treatment. *Mater. Sci. Forum* **2017**, *899*, 543–548. [[CrossRef](#)]
23. Saravana Achari, D.; Santhosh, C.; Deivasegaramani, R.; Nivetha, R.; Bhatnagar, A.; Jeong, S.K.; Grace, A.N. A non-enzymatic sensor for hydrogen peroxide based on the use of α -Fe₂O₃ nanoparticles deposited on the surface of NiO nanosheets. *Microchim. Acta* **2017**, *184*, 3223–3229. [[CrossRef](#)]
24. Yusoff, A.H.M.; Salimi, M.N.; Jamlos, M.F. A review: Synthetic strategy control of magnetite nanoparticles production. *Adv. Nano Res.* **2018**, *6*, 1–19. [[CrossRef](#)]
25. Ganapathe, L.S.; Mohamed, M.A.; Yunus, R.M.; Berhanuddin, D.D. Magnetite (Fe₃O₄) nanoparticles in biomedical application: From synthesis to surface functionalisation. *Magnetochemistry* **2020**, *6*, 68. [[CrossRef](#)]
26. de Oliveira, P.N.; Moussa, A.; Milhau, N.; Bini, R.D.; Prouillac, C.; de Oliveira, B.F.; Dias, G.S.; Santos, I.A.; Morfin, I.; Guillaume Sudre, P.; et al. In situ synthesis of Fe₃O₄ nanoparticles coated by chito-oligosaccharides: Physico-chemical characterizations and cytotoxicity evaluation for biomedical applications. *Nanotechnology* **2020**, *31*, 122890. [[CrossRef](#)]
27. Radoń, A.; Łoński, S.; Kądziołka-Gaweł, M.; Gębara, P.; Lis, M.; Łukowiec, D.; Babilas, R. Influence of magnetite nanoparticles surface dissolution, stabilization and functionalization by malonic acid on the catalytic activity, magnetic and electrical properties. *Colloids Surf. A Physicochem. Eng. Asp.* **2020**, *607*, 125446. [[CrossRef](#)]
28. da Silva, F.A.S.; Rojas, E.E.G.; Rodrigues, G.F.; da Silva, B.F.A.; de Campos, M.F. Synthesis and characterization of biocompatible Fe₃O₄ for use in cell hyperthermia. *Mater. Sci. Forum* **2014**, *775–776*, 476–481. [[CrossRef](#)]
29. Radoń, A.; Kubacki, J.; Kądziołka-Gaweł, M.; Gębara, P.; Hawełek, Ł.; Topolska, S.; Łukowiec, D. Structure and magnetic properties of ultrafine superparamagnetic Sn-doped magnetite nanoparticles synthesized by glycol assisted co-precipitation method. *J. Phys. Chem. Solids* **2020**, *145*, 109530. [[CrossRef](#)]
30. Cursaru, L.M.; Piticescu, R.M.; Dragut, D.V.; Tudor, I.A.; Kuncser, V.; Iacob, N.; Stoiciu, F. The influence of synthesis parameters on structural and magnetic properties of iron oxide nanomaterials. *Nanomaterials* **2020**, *10*, 85. [[CrossRef](#)]
31. Radoń, A.; Kądziołka-Gaweł, M.; Łukowiec, D.; Gębara, P.; Cesarz-Andraczke, K.; Kolano-Burian, A.; Włodarczyk, P.; Polak, M.; Babilas, R. Influence of magnetite nanoparticles shape and spontaneous surface oxidation on the electron transport mechanism. *Materials* **2021**, *14*, 5241. [[CrossRef](#)] [[PubMed](#)]
32. Rahmawati, R.; Permana, M.G.; Harison, B.; Nurcha; Yuliarto, B.; Suyatman; Kurniadi, D. Optimization of Frequency and Stirring Rate for Synthesis of Magnetite (Fe₃O₄) Nanoparticles by Using Coprecipitation- Ultrasonic Irradiation Methods. *Procedia Eng.* **2017**, *170*, 55–59. [[CrossRef](#)]
33. Dheyab, M.A.; Aziz, A.A.; Jameel, M.S.; Noqta, O.A.; Khaniabadi, P.M.; Mehrdel, B. Simple rapid stabilization method through citric acid modification for magnetite nanoparticles. *Sci. Rep.* **2020**, *10*, 10793. [[CrossRef](#)] [[PubMed](#)]
34. Akhirudin, N.H.M.; Shamsudin, R.; Othman, N.K. The effect of different concentrations of calcium silicate-maghemit coating towards magnetic behavior and bioactivity. *Sains Malays.* **2020**, *49*, 653–660. [[CrossRef](#)]
35. Fadli, A.; Komalasari; Adnan, A.; Iwantono; Rahimah; Addabsi, A.S. Synthesis of Magnetite Nanoparticles via Co-precipitation Method. *IOP Conf. Ser. Mater. Sci. Eng.* **2019**, *622*, 012013. [[CrossRef](#)]
36. Iacovita, C.; Florea, A.; Dudric, R.; Pall, E.; Moldovan, A.I.; Tetean, R.; Stiufluc, R.; Lucaci, C.M. Small versus large iron oxidemagnetic nanoparticles: Hyperthermia and cell uptake properties. *Molecules* **2016**, *21*, 1357. [[CrossRef](#)]
37. Kandasamy, G.; Sudame, A.; Luthra, T.; Saini, K.; Maity, D. Functionalized Hydrophilic Superparamagnetic Iron Oxide Nanoparticles for Magnetic Fluid Hyperthermia Application in Liver Cancer Treatment. *ACS Omega* **2018**, *3*, 3991–4005. [[CrossRef](#)]
38. Khairy, M. Synthesis, Characterization and Magnetic Properties of γ -irradiated and Unirradiated Magnetite Nanopowders. *Int. J. Mater. Chem.* **2013**, *3*, 106–111. [[CrossRef](#)]
39. Tajabadi, M.; Khosroshahi, M.E. Effect of Alkaline Media Concentration and Modification of Temperature on Magnetite Synthesis Method Using FeSO₄/NH₄OH. *Int. J. Chem. Eng. Appl.* **2012**, *3*, 206–210. [[CrossRef](#)]
40. Wroblewski, C.; Volford, T.; Martos, B.; Samoluk, J.; Martos, P. High yield synthesis and application of magnetite nanoparticles (Fe₃O₄). *Magnetochemistry* **2020**, *6*, 22. [[CrossRef](#)]
41. Chen, L.; Zhou, Q.; Xiong, Q.; Li, W.; Liu, J.; Yang, X. Shape-evolution and growth mechanism of fepolyhedrons. *Adv. Mater. Sci. Eng.* **2015**, *2015*, 763124. [[CrossRef](#)]
42. Lim, Y.S.; Lai, C.W.; Hamid, S.B.A.; Julkapli, N.M.; Yehya, W.A.; Karim, M.Z.; Tai, M.F.; Lau, K.S. A study on growth formation of nano-sized magnetite Fe₃O₄ via co-precipitation method. *Acta Crystallogr. Sect. A Found. Crystallogr.* **2014**, *18*, S6-457–S6-461. [[CrossRef](#)]
43. Javed, M.; Khan, A.A.; Kazmi, J.; Mohamed, M.A.; Ahmed, M.S.; Iqbal, Y. Impedance spectroscopic study of charge transport and relaxation mechanism in MnCr₂O₄ ceramic chromite. *J. Alloys Compd.* **2021**, *854*, 156996. [[CrossRef](#)]
44. Javed, M.; Khan, A.A.; Ahmed, M.S.; Khisro, S.N.; Kazmi, J.; Bilkees, R.; Khan, M.N.; Mohamed, M.A. Temperature dependent impedance spectroscopy and electrical transport mechanism in sol-gel derived MgCr₂O₄ spinel oxide. *Phys. B Condens. Matter* **2020**, *599*, 412377. [[CrossRef](#)]
45. Karim, S.S.A.; Takamura, Y.; Tue, P.T.; Tung, N.T.; Kazmi, J.; Dee, C.F.; Majlis, B.Y.; Mohamed, M.A. Developing conductive highly ordered zinc oxide nanorods by acetylacetone-assisted growth. *Materials* **2020**, *13*, 1136. [[CrossRef](#)]

46. Javed, M.; Khan, A.A.; Kazmi, J.; Mohamed, M.A.; Khan, M.N.; Hussain, M.; Bilkees, R. Dielectric relaxation and small polaron hopping transport in sol-gel-derived NiCr₂O₄ spinel chromite. *Mater. Res. Bull.* **2021**, *138*, 111242. [[CrossRef](#)]
47. Kazmi, J.; Ooi, P.C.; Raza, S.R.A.; Goh, B.T.; Karim, S.S.A.; Samat, M.H.; Lee, M.K.; Razip Wee, M.F.M.; Taib, M.F.M.; Mohamed, M.A. Appealing stable room-temperature ferromagnetism by well-aligned 1D Co-doped Zinc Oxide Nanowires. *J. Alloys Compd.* **2021**, *872*, 159741. [[CrossRef](#)]
48. Kazmi, J.; Ooi, P.C.; Goh, B.T.; Lee, M.K.; Razip Wee, M.F.M.; Karim, S.A.S.; Ali Raza, S.R.; Mohamed, M.A. Bi-doping improves the magnetic properties of zinc oxide nanowires. *RSC Adv.* **2020**, *10*, 23297–23311. [[CrossRef](#)]
49. Guo, S.; Li, D.; Zhang, L.; Li, J.; Wang, E. Monodisperse mesoporous superparamagnetic single-crystal magnetite nanoparticles for drug delivery. *Biomaterials* **2009**, *30*, 1881–1889. [[CrossRef](#)]
50. Schwaminger, S.P.; Syhr, C.; Berensmeier, S. Controlled synthesis of magnetic iron oxide nanoparticles: Magnetite or maghemite? *Crystals* **2020**, *10*, 214. [[CrossRef](#)]
51. Deivasegaramani, R.; Karunanidhi, G.; Santhosh, C.; Gopal, T.; Saravana Achari, D.; Neogi, A.; Nivetha, R.; Pradeep, N.; Venkatraman, U.; Bhatnagar, A.; et al. Chemoresistive sensor for hydrogen using thin films of tin dioxide doped with cerium and palladium. *Microchim. Acta* **2017**, *184*, 4765–4773. [[CrossRef](#)]
52. Johari, M.H.; Sirat, M.S.; Mohd Ambri Mohamed, S.; Nasir, N.F.M.; Mohd Asri Mat Teridi, A.R.M. Effects of Mo vapor concentration on the morphology of vertically standing MoS₂ nanoflakes. *Nanotechnology* **2020**, *31*, 305710. [[CrossRef](#)] [[PubMed](#)]
53. Kandasamy, G.; Maity, D. Recent advances in superparamagnetic iron oxide nanoparticles (SPIONs) for in vitro and in vivo cancer nanotheranostics. *Int. J. Pharm.* **2015**, *496*, 191–218. [[CrossRef](#)]
54. Sun, S.N.; Wei, C.; Zhu, Z.Z.; Hou, Y.L.; Venkatraman, S.S.; Xu, Z.C. Magnetic iron oxide nanoparticles: Synthesis and surface coating techniques for biomedical applications. *Chin. Phys. B* **2014**, *23*, 037503. [[CrossRef](#)]
55. Moacă, E.-A.; Coricovac, E.D.; Soica, C.M.; Pinzară, I.A.; Păcurariu, C.S.; Dehelean, C.A. Preclinical Aspects on Magnetic Iron Oxide Nanoparticles and Their Interventions as Anticancer Agents: Enucleation, Apoptosis and Other Mechanism. In *Iron Ores and Iron Oxide Materials*; IntechOpen: London, UK, 2018. [[CrossRef](#)]
56. Ghazanfari, M.R.; Kashefi, M.; Shams, S.F.; Jaafari, M.R. Perspective of Fe₃O₄ nanoparticles role in biomedical applications. *Biochem. Res. Int.* **2016**, *2016*, 7840161. [[CrossRef](#)]
57. Reyes-ortega, F.; Delgado, Á.V.; Iglesias, G.R. Modulation of the magnetic hyperthermia response using different superparamagnetic iron oxide nanoparticle morphologies. *Nanomaterials* **2021**, *11*, 627. [[CrossRef](#)]
58. Nemati, Z.; Alonso, J.; Rodrigo, I.; Das, R.; Garaio, E.; García, J.Á.; Orue, I.; Phan, M.H.; Srikanth, H. Improving the Heating Efficiency of Iron Oxide Nanoparticles by Tuning Their Shape and Size. *J. Phys. Chem. C* **2018**, *122*, 2367–2381. [[CrossRef](#)]
59. Nemati, Z.; Alonso, J.; Martinez, L.M.; Khurshid, H.; Garaio, E.; Garcia, J.A.; Phan, M.H.; Srikanth, H. Enhanced Magnetic Hyperthermia in Iron Oxide Nano-Octopods: Size and Anisotropy Effects. *J. Phys. Chem. C* **2016**, *120*, 8370–8379. [[CrossRef](#)]
60. El Ghandoor, H.; Zidan, H.M.; Khalil, M.M.H.; Ismail, M.I.M. Synthesis and some physical properties of magnetite (Fe₃O₄) nanoparticles. *Int. J. Electrochem. Sci.* **2012**, *7*, 5734–5745.
61. Mohapatra, J.; Zeng, F.; Elkins, K.; Xing, M.; Ghimire, M.; Yoon, S.; Mishra, S.R.; Liu, J.P. Size-dependent magnetic and inductive heating properties of Fe₃O₄ nanoparticles: Scaling laws across the superparamagnetic size. *Phys. Chem. Chem. Phys.* **2018**, *20*, 12879–12887. [[CrossRef](#)]
62. Goya, G.F.; Lima, E.; Arellano, A.D.; Torres, T.; Rechenberg, H.R.; Rossi, L.; Marquina, C.; Ibarra, M.R. Magnetic hyperthermia with Fe₃O₄ nanoparticles: The influence of particle size on energy absorption. *IEEE Trans. Magn.* **2008**, *44*, 4444–4447. [[CrossRef](#)]
63. Tong, S.; Quinto, C.A.; Zhang, L.; Mohindra, P.; Bao, G. Size-Dependent Heating of Magnetic Iron Oxide Nanoparticles. *ACS Nano* **2017**, *11*, 6808–6816. [[CrossRef](#)] [[PubMed](#)]
64. Nguyen, D.T.; Kim, K.-S. Controlled synthesis of monodisperse magnetite nanoparticles for hyperthermia-based treatments. *Powder Technol.* **2016**, *301*, 1112–1118. [[CrossRef](#)]
65. Cervadoro, A.; Giverso, C.; Pande, R.; Sarangi, S.; Preziosi, L.; Wosik, J.; Brazdeikis, A.; Decuzzi, P. Design Maps for the Hyperthermic Treatment of Tumors with Superparamagnetic Nanoparticles. *PLoS ONE* **2013**, *8*, e57332. [[CrossRef](#)]
66. Shi, D.; Sadat, M.E.; Dunn, A.W.; Mast, D.B. Photo-fluorescent and magnetic properties of iron oxide nanoparticles for biomedical applications. *Nanoscale* **2015**, *7*, 8209–8232. [[CrossRef](#)]